AGU PUBLICATIONS

Geophysical Research Letters

RESEARCH LETTER
10.1002/2016GL070993

Key Points:
- Macroscopic source parameters of earthquakes in the Japan subduction zone were determined using the cluster-event method
- Static stress drop increases with depth and the radiation efficiency is systematically low for earthquakes below 60 km
- Shear heating instability may be an important rupture mechanism for intermediate-depth earthquakes

Supporting Information:
- Supporting Information S1

Correspondence to:
J. Y.-T. Ko,
justinko@caltech.edu

Citation:
Ko, J. Y.-T., and B.-Y. Kuo (2016), Low radiation efficiency of the intermediate-depth earthquakes in the Japan subduction zone, *Geophys. Res. Lett.*, *43*, 11,611–11,619, doi:10.1002/2016GL070993.

Received 25 AUG 2016
Accepted 4 NOV 2016
Accepted article online 5 NOV 2016
Published online 26 NOV 2016

Low radiation efficiency of the intermediate-depth earthquakes in the Japan subduction zone

Justin Yen-Ting Ko[1] and Ban-Yuan Kuo[2]

[1]California Institute of Technology, Pasadena, California, USA, [2]Institute of Earth Sciences, Academia Sinica, Taipei, Taiwan

Abstract Robust determination of earthquake source parameters over a continuous depth range is central to inferring rupture mechanisms dominant at different depths. We employed a cluster-event method to constrain the source parameters as well as along-path attenuation for earthquakes over 0–150 km depths and 4 orders of seismic moments in the Japan subduction zone. We found that corner frequency and stress drop increase with depth, whereas the radiated energy scaled by seismic moment declines with depth slightly. As a result, the radiation efficiency exhibits a notable deficit for events deeper than 60 km. Together these suggest an increased energy dissipation during faulting in ductile deformation regime, consistent with shear heating instability as an important faulting mechanism for intermediate-depth earthquakes.

1. Introduction

Occurrence of earthquake at depths below the brittle-ductile transition requires some mechanisms to facilitate faulting under high confining pressure, but these mechanisms are not well understood. The long-time favorable hypothesis for triggering of intermediate-depth earthquakes (50–300 km) is to raise the pore pressure in the rock by breaking down hydrous minerals [*Green and Houston*, 1995]. Dehydration embrittlement has been implied from laboratory experiments [e.g., *Dobson et al*., 2002; *Jung et al*., 2004] and gained critical support from the spatial coincidence between intraslab seismicity and the predicted metamorphic reaction locations in the subducting crust and mantle [*Peacock and Wang*, 1999; *Peacock*, 2001; *Hacker et al*., 2003].

Another appealing hypothesis is shear heating instability or thermal runaway, in which viscous creep is localized along fine-grained shear zone and grows to rapid slip aided by frictional heating and melting. Grain size sensitive shear heating has been reproduced in numerical simulations [*Kelemen and Hirth*, 2007; *John et al*., 2009; *Thielmann et al*., 2015] and documented in the field as pseudotachylyte, a quenched melt on the thin fault vein exhumed from lower crustal depth in paleosubduction zones [*Anderson and Austrheim*, 2006; *Deseta et al*., 2014]. Low seismic efficiency inferred for the deep Bolivian earthquake is considered evidence for melting of a thin fault [e.g., *Kanamori et al*., 1998]. Recently, *Prieto et al*. [2013] reported high stress drop and low radiation efficiency for earthquakes in the Bucaramanga Nest (BN), Columbia, at depths of 140–170 km, favoring thermal runaway as a dominant process.

To better characterize the mechanisms of intermediate-depth earthquakes, it is beneficial to construct a continuous profile of source properties across the brittle-ductile transition depth, at about 40–70 km depending on the mantle temperature, and examine its pattern. In their study of the mantle wedge of the Japan subduction zone (JSZ), *Ko et al*. [2012] developed a cluster-event method (CEM) to suppress the source-path ambiguity and better constrain each. We expanded the data set of *Ko et al*. [2012] (Figure 1a) and employed an improved nonlinear inversion technique in the CEM. We calculated both static and dynamic source parameters for events in a depth range of 0–150 km. We find conspicuous trends of some of these parameters with depth suggesting energy dissipation in the rupture of earthquake below 60 km depth.

2. Method and Data

We solve for corner frequency f_c, scalar moment M_0, and along-path quality factor Q for earthquakes by minimizing the difference between the observed displacement spectrum and the theoretical one based on the Brune-type [*Brune*, 1970] source model $\dot{M}(f) = M_0 / \left[1 + (f/f_c)^2\right]$, where $\dot{M}$ is moment rate function and f is frequency. Earthquake parameters and waveforms were obtained from the National Research Institute for Earth Science and Disaster Resilience (NIED) catalog and F-net stations [*Okada et al*., 2004]. Here we briefly describe the routines with which P wave spectrum was determined. A 5 s window of P waveform was

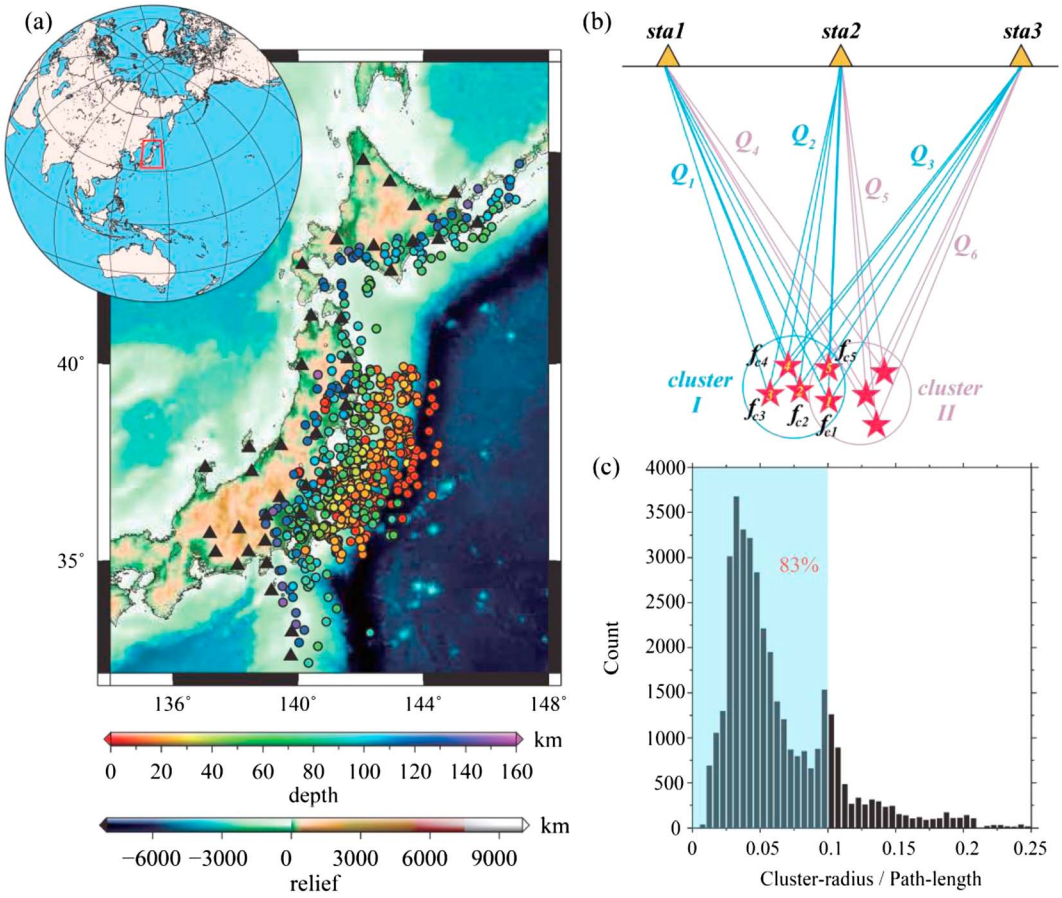

Figure 1. The investigation region and methodology synopsis. (a) Distribution of events (color-coded circles) and stations (black triangles). (b) Example of how CEM works [after *Ko et al*., 2012]. For each cluster, five f_c and three Q values are to be determined, if the cluster size is small and the paths sample essentially the same structure. The number of unknowns is reduced relative to other methods (see text). The radius of cluster is required to be one tenth of the path length between the target event and the nearest station. (c) Some events in a cluster may have shorter paths than the target event, but the data with cluster-radius/path length ratio less than one tenth comprise a dominant percentage (83%) of the data set.

extracted from vertical displacement record starting at 0.5 s before the handpicked arrival and was cosine tapered (0.5 s length) on each end. The multitaper technique [*Park et al*., 1987; *Prieto et al*., 2007; *Prieto et al*., 2009] was applied to this data window to obtain *P* wave spectrum. Noise spectrum was similarly determined from a 5 s window before and 1 s apart from the data window. Spectral fitting was performed only in the frequency band in which the *P* to noise amplitude ratio is greater than 5. The high-frequency limit is set at 8 Hz, slightly lower than the 10 Hz Nyquist frequency of the F-net data. More details of data preparation and processing can be found in *Ko et al*. [2012].

While M_0 can be determined reliably by averaging the low-frequency part of the best fit spectrum over stations, f_c and Q trade off with each other severely in the presence of noise. The CEM tackles the trade-off problem by configuring the measurements on a cluster-station basis rather than the conventional event-station basis (Figure 1b). The CEM assumes that (1) the raypaths from a cluster of events to the same station are similar and hence share an identical path effect Q and (2) only one f_c is allowed for each event in one cluster. Source directivity is ignored. *Ko et al*. [2012] demonstrated that its effect on corner frequency is $\frac{\delta f_c}{f_c} = \frac{V_r}{\alpha}\cos(\theta) + O^2$ in a simplified 2-D situation where θ is the angle between wave takeoff direction and fault rupture direction and O^2 is second-order term proportional to $\left(\frac{V_r}{\alpha}\right)^2$. Except for θ close to zero, this bias can be largely suppressed if the source is covered by a wide aperture of stations in 3-D, a case for the JSZ.

Figure 1b displays an example of a measurement on the cluster-station basis. In cluster I of 5 events received by 3 stations, there are 8 parameters to be determined from 15 sets of spectrum. In contrast, the frequently

used method in which each spectrum is fitted with a pair of f_c and Q would have 30 unknowns for 15 sets of spectrum, largely increasing the likelihood of f_c-Q trade-off. The linearized method of *Stachnik et al*. [2004] deals with the system of one event (one f_c) for many stations. In the cluster I configuration, this method involves 20 unknowns for the same amount of data. Therefore, for a cluster of K events and N stations and a total of $K \times N$ sets of data, the number of unknowns are $K+N$, $(K \times N)+K$, and $(K \times N) \times 2$ for CEM, the linearized inverse of *Stachnik et al*. [2004], and the conventional spectrum fitting, respectively. As K and $N \gg 2$ for a cluster, the CEM grows rapidly to an overdetermined inverse problem with effectively more constraints than in other methods.

The selection of clusters also faces a trade-off. More events included in a cluster better stabilize the inversion, whereas tighter clusters better satisfy the CEM basic assumption. We chose a compromise at which the radius of the cluster for the target event is taken as one tenth of the path length between the target event and the nearest station (Figure 1b). This scheme results in 83% of data with radius/path length ratio less than 0.1 (Figure 1c) and 3–10 events in a cluster. To solve this nonlinear inverse problem, the Neighborhood Algorithm (NA) [*Sambridge*, 1999] was used to drive the search in a multidimensional parameter space. See the details of CEM inversion in the supporting information.

To evaluate the performance of NA in the CEM, we conducted a synthetic test with the combination of the source and path parameters the same as in *Ko et al*. [2012]. Figure 2 illustrates that the NA steers the search iteratively toward the promising region in the model space and simultaneously increases the density of samples there. The NA is more efficient in convergence than the simulated annealing method adopted in *Ko et al*. [2012]. The CEM returns a solution identical to the input model after several iterations in all the cases in the test.

In *Ko et al*. [2012] where mantle wedge structure is the main target, only events between 70 and 150 km depths were used. We expand the data set by incorporating shallow events, including those along the plate interface. We do not analyze events deeper than 150 km, because seismic waves from deep intraslab events likely travel long enough within the slab to increase complexity and uncertainty in the path effect. The final data set consists of 813 events, 26,653 spectra, and 405 clusters for the F-net stations. These data, with a depth range of 0–150 km and a moment range 4 orders of magnitude wide or moment magnitude (M_w) range 3–6, provide an opportunity of comprehensive evaluation of source characteristics as a function of depth.

3. Results

With f_c and M_o of each event determined from the CEM, the radius of a circular fault can be estimated as $r_c = k\beta/f_c$ [*Brune*, 1970; *Madariaga*, 1976], where β is the shear wave velocity at the hypocenter given by the 3-D velocity model of *Nakamura et al*. [2008] and k is a constant of 0.32 for P waves. We fit f_c with the equation in the form of $f_c \propto {M_0}^{-1/(3+\varepsilon)}$ and found ε virtually zero, suggesting no significant deviation from self-similarity model. The static stress drop is then calculated as $\Delta\sigma_s = \frac{7}{16}\frac{M_0}{r_c^3} = \frac{7}{16} M_0 \frac{f_c^3}{(k\beta)^3}$ [*Eshelby*, 1957]. To highlight the depth dependence of the source parameters, we define three depth zones: I, 0–25 km; II, 25–60 km; and III, $>$ 60 km (Figure 3a). Figure 3b shows that $f_c \propto {M_0}^{-1/3}$ fits the data of each depth zone well and that f_c increases with depth. As a result, $\Delta\sigma_s$ is essentially invariant over M_0 in each depth zone while increases substantially with depth despite the fact that the velocity has an opposite effect (Figure 3c). Our data corroborate that intermediate-depth earthquakes in the JSZ obey self-similar processes over the moment range of this study. However, the depth dependence of f_c and $\Delta\sigma_s$ are the key to infer different faulting mechanisms at different depths.

The radiated energy is estimated by integrating the source spectrum of P wave and scaling the result for S wave [*Haskell*, 1964; *Boatwright*, 1980; *Boatwright and Fletcher*, 1984; *Venkataraman and Kanamori*, 2004a, 2004b]

$$E_R = \frac{8\pi}{15\rho\alpha^5}(1+q)\int_0^\infty f^2 \left|\dot{M}(f)\right|^2 \mathrm{d}f \tag{1}$$

where α is P wave velocity, $\dot{M}$ is the moment rate spectrum for P wave, and q is S-to-P energy ratio and is (3/2) $(\alpha/\beta)^5$ if the corner frequencies of S and $P$are identical. We removed from observed displacement spectrum the attenuation effect for each path determined by the CEM and carried out the integration between 0.2 and 8 Hz, which reflect the limitation of the 5 s window used in CEM and the Nyquist frequency of the F-net station (10 Hz). Beyond this range, the radiated energy was calculated from the CEM-determined best fit Brune's source model in 0.001–0.2 Hz and 8–100 Hz to compensate for the possible energy

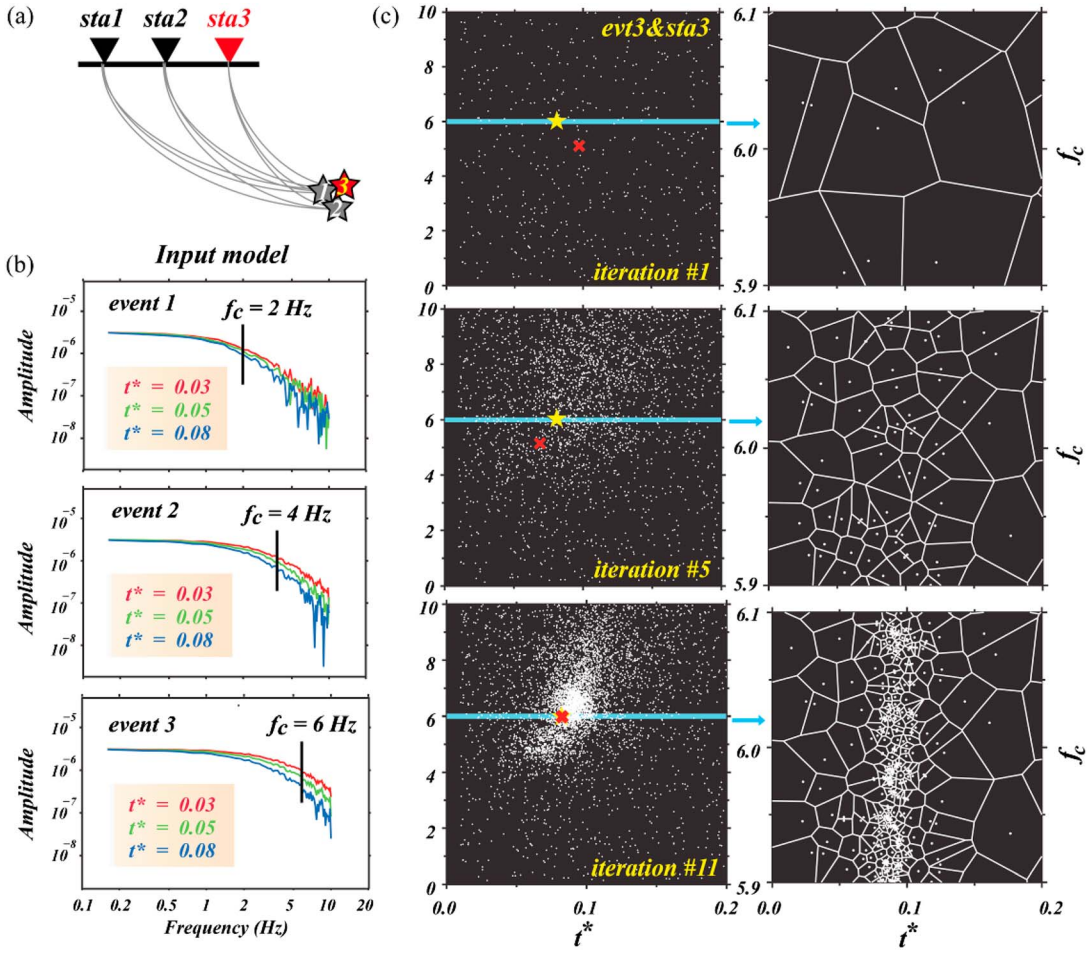

Figure 2. Synthetic test of CEM using Neighborhood Algorithm (NA) [*Sambridge*, 1999]. (a) The event cluster and stations schematics. Event 3-station 3 pair is used to highlight the performance of the NA in Figure 2c. (b) Synthetic data polluted with error with t^* and f_c annotated. t^* is the time integral of $1/Q$ along path $\left(t^* = \int \text{path} \frac{dr}{Q}\right)$, a measure of along-path attenuation. (c) Three iteration snapshots of the CEM solution for the event 3-station 3 pair in Figure 2a. The panels from top downward illustrate the evolution of the CEM solution and the Voronoi cells used in the NA in the model space. The true solution, or the input to the CEM, is $t^* = 0.08$ and $f_c = 6$ Hz (yellow star). Right column is the blowup of the blue region in the left column. The output of the CEM (red cross) converges to the true solution at eleventh iteration.

underestimation due to limited data bandwidth [*Ide and Beroza*, 2001]. The low- and high-frequency extrapolation contributes to about 15% of the total energy. In equation (1), $q \sim 23.2$ for a Poisson solid. In practice, we use the β/α from *Nakamura et al.* [2008] at each hypocentral location.

Figure 4 shows the calculated E_R scaled by seismic moment, or E_R/M_0. The scaled energy demonstrates no obvious trend with M_0, although the means of the three moment intervals, $M_0 < 10^{15}$, $10^{15} < M_0 < 10^{16}$, and $M_0 > 10^{16}$, increase with M_0 systematically (Figure 4a). E_R/M_0 appears to slightly decrease with depth, also highlighted by the means of each depth zone (Figure 4b). The means and the respective standard errors for zones I, II, and III are 3.56 ± 0.03, 3.02 ± 0.03, and 2.25 ± 0.04, each timed by 10^{-5}, respectively. The differences between these three mean values are robust.

The scaled energy integrated from the Brune-type moment rate function has an analytical form of [e.g., *Ide and Beroza*, 2001]

$$\left(\frac{E_R}{M_0}\right)^B = \frac{2\pi^2}{15\mu}\left[\left(\frac{\beta}{\alpha}\right)^5 + \frac{3}{2}\right]\frac{16}{7}k^3\Delta\sigma_s \tag{2}$$

Substituting observed values of $\Delta\sigma_s$ into equation (2) yields an evident increase in scaled energy in zone III. The measured scaled energy in zone III is considerably lower than that predicted by the Brune model (Figure 4b).

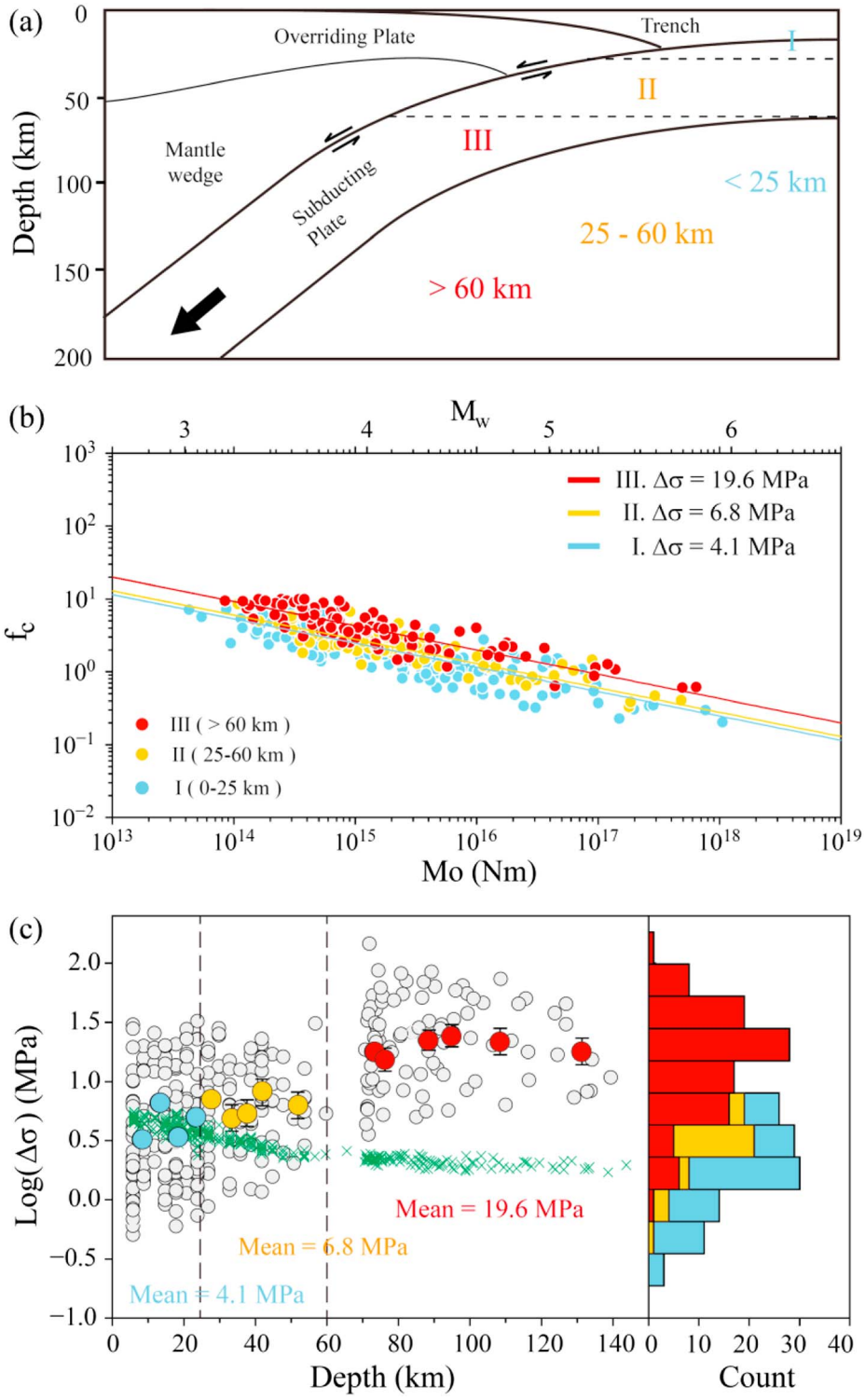

Figure 3. (a) Schematic model illustrates the subduction structure and the depth zones I, 0–25 km; II, 25–60 km; and III, > 60 km, as a scheme to reveal possible distinct rupture mechanisms. Color code is blue, yellow, and red for zones I, II, and III, throughout all the figures. (b) Measured f_c versus M_0. The total data set obeys $f_c \propto M_0^{-1/3}$, and f_c increases from zone I to zone III. (c) $\Delta\sigma_s$ versus depth (light gray circle). Colored circles are means (with standard errors) of each 5 km depth interval; if the number of data is less than 10 in an interval, the thickness increments by every 5 km until the number of data is 10 or greater, but the maximum thickness of interval is set at 30 km. The zone means of $\Delta\sigma_s$, 4.1, 6.8, and 19.6 MPa, are labeled on the figure. Crosses in green are stress drop calculated using the average f_c of zone I, emphasizing that the $\Delta\sigma_s$ increase is dictated by f_c, not velocity structure. Right panel shows the histograms of $\Delta\sigma_s$ for the three depth zones.

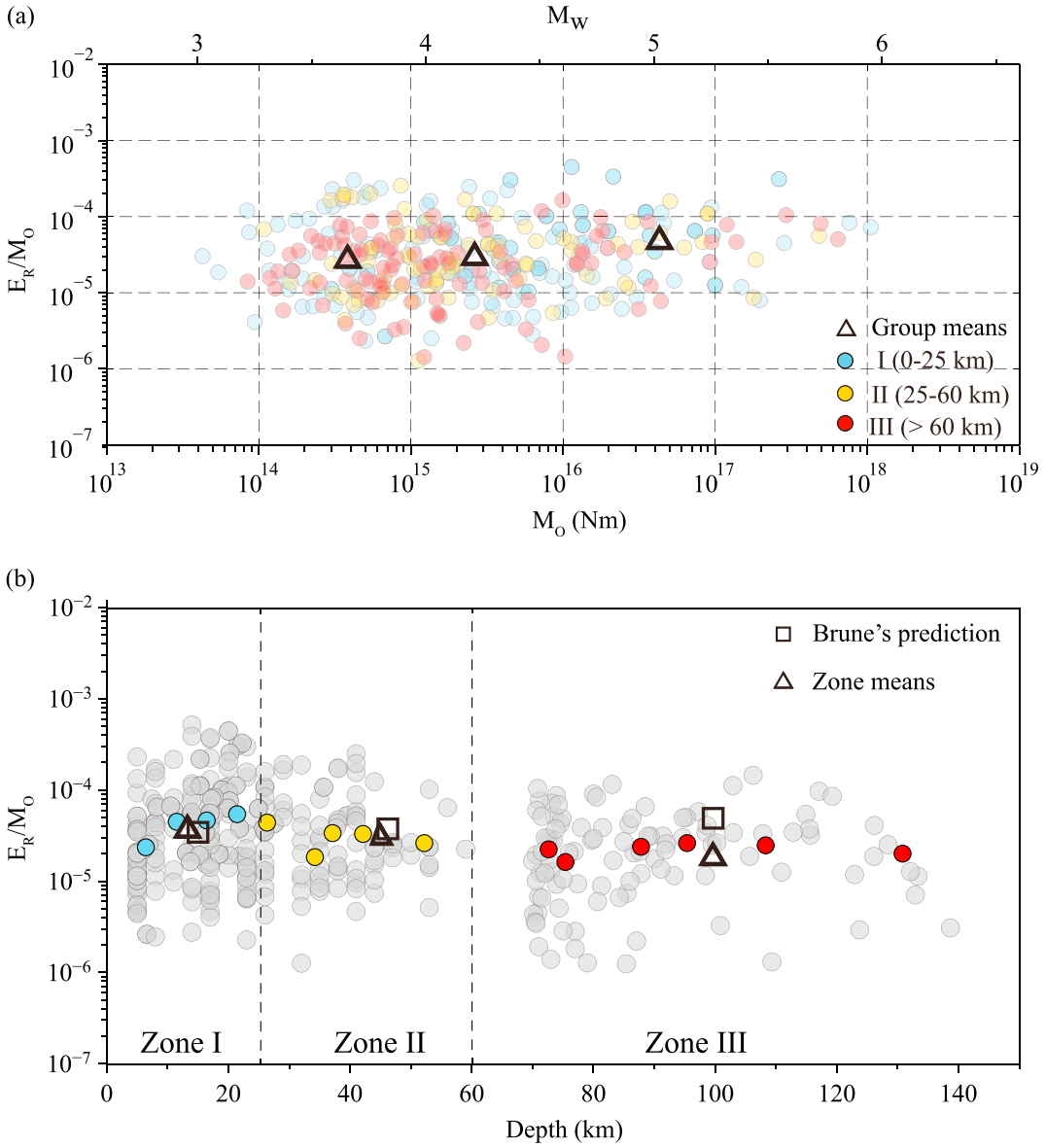

Figure 4. Observed scaled energy E_R/M_0. (a) E_R/M_0 as a function of M_0. The means and standard errors are 2.65 ± 0.08, 2.88 ± 0.05, and 5.00 ± 0.05, each timed by 10^{-5}, for the three moment intervals separated at $M_0 = 10^{15}$ and 10^{16}. These means increase with M_0, but the overall trend is weak. (b) E_R/M_0 as a function of depth. Data points and means over depth intervals are plotted in the same way as Figure 3c. The means of each depth zone (triangles) are 3.56, 3.02, and 2.25, with standard errors of 0.003, 0.005, and 0.007, respectively, all multiplied by 10^{-5}, for zones I, II, and III. The means of each zone predicted by Brune's source model, i.e., $(E_R/M_0)^B$, are plotted in square. The measured E_R/M_0 (triangle) relative to $(E_R/M_0)^B$ (square) in zone III represents the deficiency of converting stress drop to radiated energy for intermediate-depth earthquakes.

We calculated the radiation efficiency as [e.g., *Venkataraman and Kanamori*, 2004a]

$$\eta_R = 2\left(\mu \frac{E_R}{M_0}\right)\frac{1}{\Delta\sigma_s} \tag{3}$$

The means of η_R for zones I, II, and III are 0.34 ± 0.02, 0.36 ± 0.03, 0.27 ± 0.03, respectively. We observe a notable decrease of η_R in zone III relative to that in the above zones (Figure 5). The Brune source model predicts a theoretical radiation efficiency of

$$\eta_R^B = \frac{4\pi^2}{15}\left[\left(\frac{\beta}{\alpha}\right)^5 + \frac{3}{2}\right]\frac{16}{7}k^3 \tag{4}$$

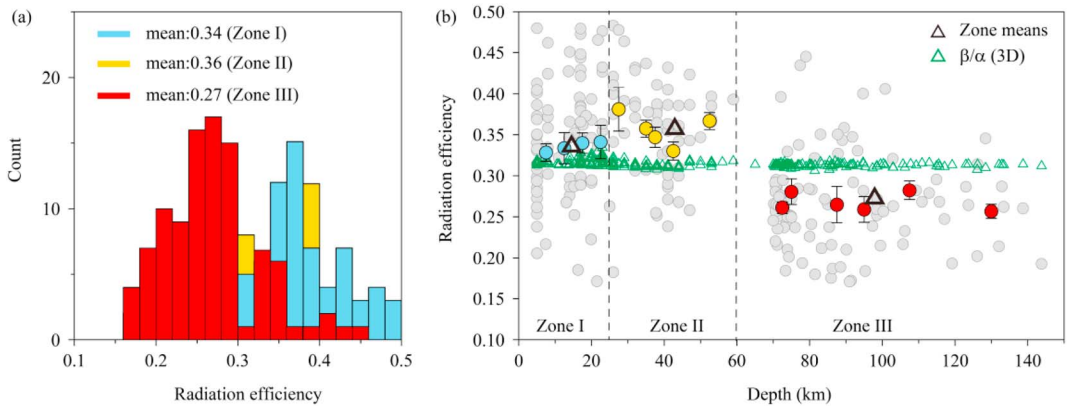

Figure 5. Radiation efficiency η_R. (a) Histograms of η_R in three depth zones and their means, 0.34, 0.36, and 0.27, respectively. (b) η_R as a function of depth. Each data points are in gray circle. Data points and means over depth intervals are plotted in the same way as Figure 3c. The standard error of the means is shown. The radiation efficiency predicted from the Brune-type source model η_R^B is denoted by triangles in green. The discrepancy between η_R and η_R^B and the low η_R in zone III argue for the presence of a dissipative faulting mechanism in zone III.

which is a function of velocity structure only. The comparison between η_R and η_R^B (Figure 5) suggests that the observed reduction from zones II to III cannot be an artifact of velocity structures but instead may represent a fundamental difference in source mechanism prevalent in the brittle and ductile deformation regimes.

4. Discussion and Conclusion

We show robust evidence for source self-similarity in the measured f_c and $\Delta\sigma_s$ for the seismic moment and depth ranges of earthquakes in the JSZ. *Allmann and Shearer* [2009] documented a global feature that stress drop does not vary with event size for moderate to large earthquakes. However, in BN, *Prieto et al.* [2013] found an increase in stress drop with M_0 in the nest's narrow seismicity depth range. Nonsimilarity may manifest in different forms. *Poli and Prieto* [2014] revealed that the source duration $\left(\propto \frac{1}{f_c}\right)$ deviates substantially from the one third rule with M_0 for both intermediate-depth and deep-focus earthquakes. *Denolle and Shearer* [2016] found that double corner frequencies may exist and progressively dominate from small to large shallow thrust events, suggesting non-self-similar rupture behavior, while $\Delta\sigma_s$ and E_R/M_0 remain invariant with event size in compliance with self-similarity. Most of recent studies show little dependence of E_R/M_0 on M_0 for large shallow and deep earthquakes [*Tocheport et al.*, 2007; *Baltay et al.*, 2010; *Baltay et al.*, 2014]. Although an incremental increase of E_R/M_0 with M_0 is presented, our data can be explained by a constant as well, in general agreement with self-similar scaling. Whether these disparities stem from differences in methods, tectonic regions, focal depths, seismic moment ranges, or earthquake types remain to be explored.

The macroscopic source parameters determined in this study may be biased if some of the hidden assumptions are oversimplified. The rejection of structure-dominant η_R exercised above rests on the assumption of a constant q. It is much less of a concern in other studies in which radiated energy is estimated based mainly on S wave [e.g., *Prieto et al.*, 2004]. A range of q values from 9 to about 30 has been reported [e.g., *Prieto et al.*, 2004; *Venkataraman and Kanamori*, 2004b; *Viegas et al.*, 2010], and its depth dependence is unknown. To erase the deficit of η_R in zone III, q has to increase in order to magnify the energy estimates with depth. Consideration of corner frequency shift between P and S lowers the q value [*Boatwright and Fletcher*, 1984]. A possible scenario to increase q is to start with a corner frequency shift and allow it to diminish with depth. At present no physical or observational ground exists to help assess this scenario.

Another source of concern is rupture velocity V_r. The coefficient k of 0.32 given by *Madariaga* [1976] is based on a constant V_r/β of 0.9, and k decreases with V_r/β. For a measured f_c, or equivalently a fixed source duration, lower V_r entails smaller fault dimension r_c, and this is achieved via a smaller k value in the equation $r_c = k\beta/f_c$. If V_r/β is actually lower than 0.9 at depths but $k = 0.32$ is still used, $\Delta\sigma_s = \frac{7}{16} M_0 \frac{f_c^3}{(k\beta)^3}$ is underestimated. There is evidence that rupture velocities may reduce to 0.2–0.6 β for large deep earthquakes in

subduction zones in general with exceptions at particular depth range [*Park and Mori*, 2008; *Suzuki and Yagi*, 2011]. Slower V_r could happen in zone III because lower η_R implies rupture being slowed down to counter fracture energy [e.g., *Kanamori and Brodsky*, 2004]. It is possible that the η_R deficit in zone III may be even more pronounced.

Nishitsuji and Mori [2013] reported radiation efficiency ranging from 0.01 to over 1 for earthquakes at 65–150 km depths in northeast Japan. They found that, statistically, intermediate-depth earthquakes have lower η_R than shallow earthquakes. However, the data used in *Nishitsuji and Mori* [2013] scatter substantially, and the comparison with shallow events is made between results obtained with different methods across different regions. Although absolute values of energy and radiation efficiency presented in this study depend on q, a continuous profile of source parameters renders an unambiguous illustration of the η_R deficit associated with intermediate-depth earthquake relative to shallow ones.

The variations in the macroscopic source properties across the 60 km depth in the JSZ is akin to the findings at the BN [*Prieto et al*., 2013]. The combination of high stress drop and extremely low radiation efficiency, i.e., 0.02, in the BN leads to the assertion that shear heating instability, or thermal runaway, plays a major role in rupturing of intermediate-depth earthquakes [*Prieto et al*., 2013]. In the JSZ, although the scaled energy declines with depth only mildly, it is considerably lower than what the stress drop can cause in zone III (Figure 4b). The macroscopic parameters together may signify the inception of a dissipative faulting mechanism in the ductile deformation regime. It is consistent with the shear heating instability as a control process during faulting but does not rule out other processes that might be triggered by dehydration reaction in the subduction zone [e.g., *Wibberley and Shimamoto*, 2005; *Schmitt et al*., 2011].

The low efficiency in converting stress drop to radiated energy in zone III suggests that the *P* wave spectral amplitude may be lower than that of the Brune's model somewhere along the spectrum. In the calculation of equation (1), the data moment rate function at the high and low frequencies is simulated by the Brune's moment rate function, and thus, the energy shortage cannot be contributed from the two ends. One possible scenario is that the dissipation process causes loss of energy in the vicinity of corner frequency, while the overall spectral shape can still be fitted by the Brune-type source with an f^{-2} falloff. This is different from the presence of intermediate falloff rate of f^{-1} that *Denolle and Shearer* [2016] found to characterize the systematically less sharp spectral corner for large shallow thrust earthquakes because this intermediate falloff zone vanishes when magnitude reduces to 6 or less. Quantitatively addressing where the energy deficit might be located and how it is related to rupturing processes requires an independent effort and is beyond the scope of this paper.

Although a comparison in absolute value of η_R of this study with that in BN is premature because different methods are used, it is nonetheless worth noting that the seismogenic environments in the two regions may be fundamentally different. In the JSZ, intraslab events probably initiated as viscous creep along preexisting rupture zones in response to bending/unbending and buoyancy forces acting along the slab as a stress guide. In the BN, high-level seismicity is concentrated in a compact volume at depth 140–170 km, isolated from shallow seismicity. The tectonic origin of BN is controversial but likely related to slab detachment or lateral collision [e.g., *Zarifi et al*., 2007; *Prieto et al*., 2012]. Moreover, repeating earthquake sequences have been identified as common activities in the BN, whereas in the JSZ repeating earthquakes were rarely documented at depths greater than 50 km. How the ambient stress of the slab influences the mechanical behaviors of intraslab earthquakes requires further investigations.

Acknowledgments
The authors thank Germán Prieto, Marine Denolle, and Editor Jeroen Ritsema for their critical questions and constructive comments, which much improved the revised manuscript. The authors are grateful to Hirro Kanamori for many useful discussions. The broadband seismic records were provided by F-net (http://www.fnet.bosai.go.jp/top.php) operated by National Research Institute for Earth Science and Disaster Resilience (NIED). The research was supported by Academia Sinica Thematic Project 2015-2017 and the Ministry of Science and Technology (MOST) of Taiwan under grant MOST-104-2116-M-001-024.

References

Allmann, B. P., and P. M. Shearer (2009), Global variations of stress drop for moderate to large earthquakes, *J. Geophys. Res.*, *114*, B01310, doi:10.1029/2008JB005821.

Anderson, T. B., and H. Austrheim (2006), Fossil earthquakes recorded by pseudotachylytes in mantle peridotite from the Alpine subduction complex of Corsica, *Earth Planet. Sci. Lett.*, *242*, 58–72, doi:10.1016/j.epsl.2005.11.058.

Baltay, A. S., G. C. Beroza, and S. Ide (2014), Radiated energy of great earthquakes from teleseismic empirical Geen's function devonvolution, *Pure Appl. Geophys.*, *171*, 2841–2862.

Baltay, A., G. Prieto, and G. C. Beroza (2010), Radiated seismic energy from coda measurements and no scaling in apparent stress with seismic moment, *J. Geophys. Res.*, *115*, B08314, doi:10.1029/2009JB006736.

Boatwright, J. (1980), A spectral theory for circular seismic sources: Simple estimates of source dimension, dynamic stress drop, and radiated seismic energy, *Bull. Seismol. Soc. Am.*, *70*, 1–27.

Boatwright, J., and J. B. Fletcher (1984), The partition of radiated energy between *P* and *S* waves, *Bull. Seismol. Soc. Am.*, *74*, 361–376.

Brune, J. (1970), Tectonic stress and spectra of seismic shear waves from earthquakes, *J. Geophys. Res.*, *75*, 4997–5009, doi:10.1029/JB075i026p04997.
Denolle, M. A., and R. M. Shearer (2016), New perspectives on self-similarity for shallow thrust earthquakes, *J. Geophys. Res. Solid Earth*, *121*, 6533–6565, doi:10.1002/2016JB013015.
Deseta, N., L. D. Ashwal, and T. B. Anderson (2014), Initiating intermediate-depth earthquakes: Insights from a HP-LT ophiolite from Corsica, *Lithos*, *205–207*, 127–146, doi:10.1016/j.liths.2014.07.022.
Dobson, D. P., P. G. Meredith, and S. A. Boon (2002), Simulation of subduction zone seismicity by dehydration of serpentine, *Science*, *298*, 1407–1410.
Eshelby, J. D. (1957), The determination of the elastic field of an ellipsoidal inclusion, and related problems, *Proc. R. Soc. London, Ser. A*, *241*, 376–396.
Green, H. W., and H. Houston (1995), The mechanics of deep earthquakes, *Annu. Rev. Earth Planet. Sci.*, *23*, 169–213.
Hacker, B. R., S. M. Peacock, G. A. Abers, and S. D. Holloway (2003), Subduction factory: 2. Are intermediate-depth earthquakes in subducting slabs linked to metamorphic dehydration reactions?, *J. Geophys. Res.*, *108*(B1), 2030, doi:10.1029/2001JB001129.
Haskell, N. (1964), Radiation pattern of surface waves from point sources in a multi-layered medium, *Bull. Seismol. Soc. Am.*, *54*, 377–393.
Ide, S., and G. C. Beroza (2001), Does apparent stress vary with earthquake size?, *Geophys. Res. Lett.*, *28*, 3349–3352, doi:10.1029/2001GL013106.
John, T., S. Medvedev, L. H. Rupke, T. B. Anderson, Y. Y. Podladchikov, and H. Austrheim (2009), Generation of intermediate-depth earthquakes by self-localizing thermal runaway, *Nat. Geosci.*, *2*, 137–140, doi:10.1038/NGEO419.
Jung, H., H. W. Green II, and L. F. Dobrzhinetskaya (2004), Intermediate-depth earthquake by dehydration embrittlement with negative volume change, *Nature*, *428*, 545–549.
Kanamori, H., and E. E. Brodsky (2004), The physics of earthquakes, *Rep. Prog. Phys.*, *67*, 1429–1496.
Kanamori, H., D. Anderson, and T. H. Heaton (1998), Frictional melting during the rupture of the 1994 Bolivian earthquake, *Science*, *279*, 839–842.
Kelemen, P. B., and G. Hirth (2007), A periodic shear-heating mechanism for intermediate-depth earthquakes in the mantle, *Nature*, *446*, 787–790, doi:10.1038/nature05717.
Ko, Y. T., B. Y. Kuo, and S. H. Hung (2012), A robust determination of earthquake source parameters and mantle attenuation, *J. Geophys. Res.*, *117*, B04304, doi:10.1029/2011JB008759.
Madariaga, R. (1976), Dynamics of an expanding circular fault, *Bull. Seismol. Soc. Am.*, *66*, 639–666.
Nakamura, M., et al. (2008), Three-dimensional *P*- and *S*-wave velocity structures beneath Japan, *Phys. Earth Planet. Int.*, *168*, 49–70.
Nishitsuji, Y., and J. Mori (2013), Source parameters and radiation efficiency for intermediate-depth earthquakes in Northeast Japan, *Geophys. J. Int.*, *196*(2), 1247–1259, doi:10.1093/gji/ggt458.
Okada, Y., K. Kasahara, S. Hori, K. Obara, S. Sekiguchi, H. Fujiwara, and A. Yamamoto (2004), Recent progress of seismic observation networks in Japan Hi-net, F-net, K-NET and KiK-net, *Earth Planets Space*, *56*, 15–28.
Park, J., C. Lindberg, and F. Vernon (1987), Multitaper spectral analysis of high-frequency seismograms, *J. Geophys. Res.*, *92*, 12,675–12,648, doi:10.1029/JB092iB12p12675.
Park, S. C., and J. Mori (2008), Rupture velocity estimation of large deep-focus earthquakes surrounding Japan, *J. Geophys. Res.*, *113*, B08303, doi:10.1029/2007JB005434.
Peacock, S. M. (2001), Are lower planes of double-seismic zones caused by serpentine dehydration in subducting oceanic mantle?, *Geology*, *29*, 299–302.
Peacock, S. M., and K. Wang (1999), Seismic consequences of warm versus cool subduction metamorphism: Examples from southwest and northeast Japan, *Science*, *286*, 937–939.
Poli, P., and G. Prieto (2014), Global and along-strike variations of source duration and scaling for intermediate-depth and deep-focus earthquakes, *Geophys. Res. Lett.*, *41*, 8315–8324, doi:10.1002/2014GL061916.
Prieto, G. A., P. M. Shearer, F. L. Vernon, and D. Kilib (2004), Earthquake source scaling and self-similarity estimation from stacking *P* and *S* spectrum, *J. Geophys. Res.*, *109*, B08310, doi:10.1029/2004JB003084.
Prieto, G. A., R. L. Parker, D. J. Thomson, F. L. Vernon, and R. L. Graham (2007), Reducing the bias of multitaper spectrum estimates, *Geophys. J. Int.*, *171*, 1269–1281.
Prieto, G. A., R. L. Parker, and F. L. Vernon III (2009), A Fortran 90 library for multitaper spectrum analysis, *C. R. Geosci.*, *35*, 1701–1710.
Prieto, G. A., G. Beroza, S. A. Barrett, G. A. Lopez, and M. Florez (2012), Earthquake nests as natural laboratories for the study of intermediate-depth earthquakes mechanics, *Tectohophysics*, *570–571*, 42–56, doi:10.1016/j.tecto.2012.07.019.
Prieto, G. A., M. Florez, S. A. Barrett, G. C. Beroza, P. Pedraza, J. F. Blanco, and E. Poveda (2013), Seismic evidence for thermal runaway during intermediate-depth earthquake rupture, *Geophys. Res. Lett.*, *40*, 6064–6068, doi:10.1002/2013GL058109.
Sambridge, M. (1999), Geophysical inversion with a neighborhood algorithm—I. Searching a parameter space, *Geophys. J. Int.*, *138*, 479–494.
Schmitt, S. V., P. Segall, and T. Masuzawa (2011), Shear heating-induced thermal pressurization during earthquake nucleation, *J. Geophys. Res.*, *116*, B06308, doi:10.1029/2010JB008035.
Stachnik, J. C., G. A. Abers, and D. H. Christensen (2004), Seismic attenuation and mantle wedge temperature in the Alaska subduction zone, *J. Geophys. Res.*, *109*, B10304, doi:10.1029/2004JB003018.
Suzuki, M., and Y. Yagi (2011), Depth dependence of rupture velocity in deep earthquakes, *Geophys. Res. Lett.*, *38*, L05308, doi:10.1029/2011GL046807.
Thielmann, M., A. Rozel, B. J. P. Kaus, and Y. Ricard (2015), Intermediate-depth earthquake generation and shear zone formation caused by grain size reduction and shear heating, *Geology*, *43*, 791–794, doi:10.1130/G36864.1.
Tocheport, A., L. Rivera, and S. Chevrot (2007), A systematic study of source time functions and moment tensors of intermediate and deep earthquakes, *J. Geophys. Res.*, *112*, B07311, doi:10.1029/2006JB004534.
Venkataraman, A., and H. Kanamori (2004a), Observational constraints on the fracture energy of subduction zone earthquakes, *J. Geophys. Res.*, *109*, B05302, doi:10.1029/2003JB002549.
Venkataraman, A., and H. Kanamori (2004b), Effect of directivity on estimates of radiated seismic energy, *J. Geophys. Res.*, *109*, B04301, doi:10.1029/2003JB002548.
Viegas, G., R. E. Abercrombie, and W. Y. Kim (2010), The 2002 *M*5 Au Sable Forks, NY, earthquake sequence: Source scaling relationship and energy budget, *J. Geophys. Res.*, *115*, B07310, doi:10.1029/2009JB006799.
Wibberley, C. A. J., and T. Shimamoto (2005), Earthquake slip weakening and asperities explained by thermal pressurization, *Nature*, *436*, 689–692, doi:10.1038/nature03901.
Zarifi, Z., J. Havskov, and A. Hanyga (2007), An insight into the Bucaramanga nest, *Tectonophysics*, *443*, 93–105.